



Provided by the author(s) and University of Galway in accordance with publisher policies. Please cite the published version when available.

Title	Thermomechanical modelling for the linear friction welding process of Ni-based superalloy and verification
Author(s)	Okeke, Saviour I.; Harrison, Noel M.; Tong, Mingming
Publication Date	2020-01-22
Publication Information	Okeke, Saviour I., Harrison, Noel, & Tong, Mingming. (2020). Thermomechanical modelling for the linear friction welding process of Ni-based superalloy and verification. Proceedings of the Institution of Mechanical Engineers, Part L: Journal of Materials: Design and Applications, 234(5), 796-815. doi:10.1177/1464420719900780
Publisher	SAGE Publications
Link to publisher's version	https://doi.org/10.1177/1464420719900780
Item record	http://hdl.handle.net/10379/16805
DOI	http://dx.doi.org/10.1177/1464420719900780

Downloaded 2024-04-26T11:28:36Z

Some rights reserved. For more information, please see the item record link above.



Thermomechanical modelling for the linear friction welding process of Ni-based superalloy and verification

S.I. Okeke ^{1,3*}, N. Harrison^{1,2,3}, M. Tong^{1,2,3}

¹Mechanical Engineering, National University of Ireland Galway, Ireland.

²I-Form Advanced Manufacturing Research Centre, Ireland.

³Ryan Institute, National University of Ireland Galway, Ireland.

*Corresponding author.

Email address: S.Okeke1@nuigalway.ie (Saviour Okeke)

Abstract

This paper presents a fully coupled thermomechanical model for the linear friction welding process of Inconel-718 nickel-base superalloy by using the finite element method. Friction heat, plastic work, and contact formulation were taken into account for two deformable plastic bodies oscillating relative to each other under large compressive force. The modelling results of the thermal history at the weldline interface and thermal field at a distance away from the rubbing surfaces were compared to instrumented data sourced from related publications for model verification. Optimal LFW process parameters were identified via comparison of weld temperature to the liquidus temperature of Inconel-718 (IN718) alloy. Comparison of interface temperature showed a consistent range of values above the solidus melting temperature (1250 °C) and below the liquidus melting temperature (1360 °C) of Inconel-718 alloy. For the first time, a visible linear friction welding process window is identified using a thermomechanical computational modelling method. Through computational modelling, the influence of welding process parameters on the heat transfer and deformation of weld was systematically investigated.

Keywords

Arbitrary Lagrangian-Eulerian (ALE), linear friction welding, process window, Inconel 718, blisk, parameter optimisation

Highlights

- A fully coupled thermomechanical finite element computational model for linear friction welding (LFW) was applied to a nickel-base alloy weld.
- The finite element model has been verified by related experimental results for LFW from publications.
- The thermomechanical modelling systematically predicted the influence of process parameters on the result of welding, and the process window indicated both optimal and sub-optimal outcomes for the LFW of Inconel-718 alloy.

Abbreviations and acronyms

Nomenclature						
A_0	mm	Oscillating amplitude	Greek		Abbreviations	
c_p	J/(kg.K)	Specific heat	δ	Delta phase	ALE	Arbitrary Lagrangian-Eulerian
E	MPa	Elastic modulus	ε	Emissivity coefficient	BM	Base metal
f_0	Hz	Oscillating frequency	ε_p	Plastic strain	FE	Finite element
h_{conv}	W/(m ² .k)	Convective heat coefficient	$\dot{\varepsilon}_p$	Plastic strain rate	FEA	Finite element analysis
k	W/(m ² .k)	Thermal conductivity	γ'	Gamma prime precipitate	FEM	Finite element method
L_a	mm	Burn-off length	γ''	Gamma double prime precipitate	FIZ	Friction interface zone
m		Tresca friction factor	μ	Friction coefficient	HAZ	Heat affected zone
Q_{SPI}	W/m ²	Specific heat input	ρ	Density [kg/m ³]	IFW	Inertia friction welding
p_n	MPa	Normal pressure	τ_{fr}	Frictional shear stress [MPa]	LFWed	Linear friction welded
T_{solid}	°C	Solidus temperature	τ_{max}	Maximum frictional stress [MPa]	LFW	Linear friction welding
T_{liq}	°C	Liquidus temperature	σ	Stefan-Boltzmann constant [W/m ² K ⁴]	PEEQ	Equivalent plastic strain
T_{ref}	°C	Reference/room temperature	σ_y	Yield strength [MPa]	TMAZ	Thermomechanically-affected zone
v_0	m/s	Relative velocity			HV	Vickers Pyramid Number

1. Introduction

Linear friction welding (LFW) is an energy-efficient, highly precise, and automated solid-phase joining technique that does not involve melting of the parent alloy material. During LFW, the workpieces rub against each other rapidly, which generates heat and forms local plastic zones at the weld interface^{1,2}. When the interface material is sufficiently softened, it is extruded as a flash along the direction of reciprocation. With flash formation, burn-off lengths are clear and workpiece length is shortened along the axis of applied pressure.

The LFW configuration is such that a clamped oscillating workpiece rubs rapidly against another clamped stationary workpiece, while subjected to large compressive force³. Four recognised phases of friction welding in order of occurrence are initial, transition, equilibrium, and forging/deceleration phases. The first three phases establish transient temperature evolution and plastic deformation, and the last phase ensures bond consolidation during the application of forging pressure. LFW typically lasts between 3 s to 100 s depending on the welding process parameters implemented⁴⁻⁷.

Friction welding technology does not require filler metal addition or protective gas shielding for joining similar and dissimilar materials^{2, 8-10}. LFW process offers multiple advantages over other mechanical joining techniques, for example, fusion welding^{8, 11-13}, as it can effectively avoid the welding defects like hot cracking and it has a lower possibility for the occurrence of dissolution of hardening precipitates^{9, 10, 14} for precipitate hardened alloys. Metals and thermoplastics have been joined in multiple variations, particularly non-axisymmetric configurations, using LFW in aerospace and automotive industrial applications¹². LFW process is highly economical in terms of energy cost and energy consumption as it can effectively improve the manufacturing competitiveness of the industry and avoid negative environmental impact¹⁵.

To date, the foremost application of LFW application is in the manufacture and repair of integrally bladed disks (blisks) shown in Fig. 1¹⁶⁻¹⁸. Blisks are critical components of axial-flow compressors of gas turbine engines. The primary concern during the manufacture of blisks and other aero-engine components is obtaining appropriate material microstructure

by using optimal process parameters of the employed manufacturing techniques^{9, 10, 14}. During LFW process, the temperature and plastic deformation of the weld can affect the material microstructure and mechanical properties¹⁹⁻²¹. There is a high demand in using computational methods to predict the material thermal processes and material deformation²²⁻²⁴. So far, there has been extensive research on LFW, in relation to such as the study on the welding processes²⁵⁻²⁹, microstructural characterisation³⁰⁻³³, numerical simulation^{11, 34-39}, and analytical computation^{35, 40-43}.

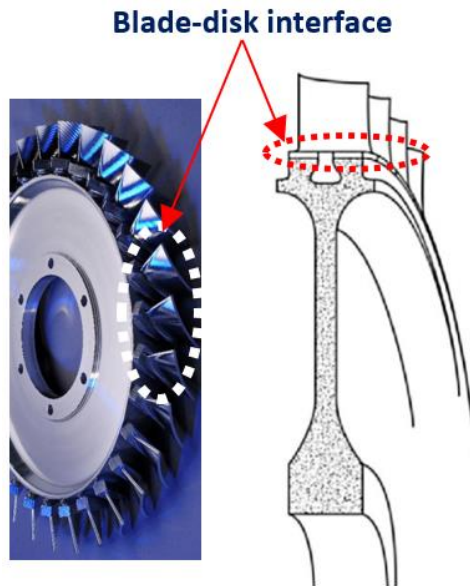


Figure 1. Linear friction welded integrally bladed-disk (blisk) manufactured at TWI^{2, 44}

Geng et al.³² measured the microhardness and averaged grain size at the GH4169 superalloy weld joint manufactured by using LFW. Because the weld interface temperature could not be measured in situ without damaging the instrument, thermocouples were positioned 5.0 mm away from the weld line interface. This meant that the influence of temperature on the weld joint had to be determined by microstructural characterisation and interface transient thermal history was predicted by finite element analysis (FEA). Wang et al.⁴⁵ examined the microstructure and mechanical properties of Ti-6.5Al-3.5Mo-1.5Zr-

0.3Si linear friction welded joint at the weld centre zone (WCZ) and thermomechanically affected zone (TMAZ). Although the relationship between shear velocity and friction pressure was described as it influences the WCZ and TMAZ, no mention was made of the contribution of the thermal field distribution to changes in WCZ and TMAZ during LFW.

Vishwakarma et al.⁹ noted that multiple LFW experiments were conducted to achieve complete joining along the weld line interface of IN718 ALVAC alloy. They observed the difference in bonding when LFW was conducted by using two different input welding parameter case studies. In one setup, the friction pressure of 70 MPa and oscillating frequency of 30 Hz were utilised, and bonding occurred only at the central region of weldline without any bonding around the workpiece periphery. In another setup, a friction pressure of 100 MPa and an oscillating frequency of 40 Hz resulted in bonding at the central weld region and workpiece periphery. The use of computational modelling can determine optimal input LFW process parameters to achieve complete bonding from the central weld region to the periphery of workpieces along the weld interface^{46,47}.

Many of the research efforts on computational modelling for the macroscopic processes of the LFW process have presented various combinations of welding process parameters. These reports have investigated the influence of heat transfer and deformation of the weld by utilising three key process parameters, which are: friction pressure, oscillation frequency, and oscillation amplitude. They are often expressed together as the specific heat input, Q_{SPI} according to Eqn. 1.

$$Q_{SPI} = \frac{p_f f_0 A_0}{2\pi} \quad (1)$$

where p_f is the friction pressure, f_0 is the oscillation frequency, and A_0 is the oscillation amplitude. Occasionally, the upset and burn-off lengths are taken into account as influencing parameters for LFW numerical procedures and experimental designs.

Commercially available finite element software packages have been used extensively such as ABAQUS, DEFORM, and ANSYS. Regarding geometric models, there are concerns on the choice of scale, dimension of workpieces, and acceptable level of simplification—

mechanical constraints and thermal mechanisms. A simplified two-dimensional (2D) finite element (FE) model that accounts for thermo-mechanical deformation in only one deformable workpiece has been reported^{34, 37, 48}. Two-dimensional (2D) models require less computational cost when compared to 3D models. However, some studies^{2, 30, 49-51} have shown that the flash morphology and the total shortening length are asymmetric for both rubbing workpieces and are best observed in a three-dimensional model compared to a two-dimensional model. To date, there is little work done on 3D modelling of LFW and much fewer publications on 3D modelling of the LFW of IN718 superalloy^{27, 44, 48, 50-54}. In this paper, the 3D computational modelling approach was investigated using a high-performance computing platform, to accurately predict the influence of welding process parameters on heat transfer and deformation of the weld during LFW.

In some publications, only the thermal process analysis of LFW was considered^{20, 42}, which is best suited for predicting transient temperature history during LFW. Bertrand et al.⁵⁵ have compared a thermal model to an oscillating thermomechanical model, where both models calculated approximately the same temperature evolution. However, only the oscillating model showed the effect of stress-induced plastic deformation. Several studies have conducted sequentially coupled thermal-mechanical modelling^{36, 48}, which shows similar transient thermal fields as a thermal model and ignores the simultaneous contribution of both thermal and mechanical fields to the plastic deformation during LFW process simulation.

Multiple finite element (FE) modelling studies on the variants of friction welding have used either Lagrangian^{48, 56}, Eulerian⁵⁷, or Lagrangian-Eulerian⁵⁸⁻⁶⁰ numerical solvers. These choices of numerical procedure are aimed at resolving numerical difficulties in contact formulations and overcoming high-strain distortion of computation mesh domain. To address the challenge of excessive element distortion during friction process simulation, Li et al.³⁷ developed Python scripts that implement mesh mapping in the Abaqus/Standard solver. To run effectively, a dedicated software package Hyperworks was used to import/export a modified orphan for the re-mesh procedures. However, in Yang et al.³⁴ the dynamic remeshing capability of Abaqus/Explicit was employed to overcome mesh distortion challenges. Further, the benefit of using arbitrary Lagrangian-Eulerian (ALE)

remeshing capability in an explicit solver comes with significant computational cost. In Abaqus/Explicit solver, for instance, the true physical time scales per numerical procedure would require between 50 h to several weeks to implement, hence many authors have reported the use of mass scaling, whose effects if wrongly specified, can decrease the overall accuracy of the numerical procedure⁶¹. The choice of a suitable numerical solver has been considered in the current research.

Frictional heating mechanism at the weld interface plays a principal role in the overall LFW process. Although many reports have proposed different friction model behaviour, it remains a subject of contention, more so that local deformation, interface temperature, slip rate, contact pressure, and lubrication effects all contribute to influencing the contact friction between rubbing workpieces. FE friction contact models are defined using a constant or variable-dependent friction coefficient value. One such influencing physical variable is temperature. The temperature-dependent coefficient of friction—to account numerically for heat generation during the welding process—is a dominant approach in the literature^{49, 51, 55, 62-65}.

A renowned source of material friction model data is the friction and wear experiments, specifically targeted at the alloy material^{34, 37, 44, 66}. While temperature-dependent friction coefficient for aluminium, titanium and steel alloys are readily available and simple to implement in computational modelling tools^{27, 46, 67-70}, this is not the situation for several nickel-base alloys. Most of the experimentally derived nickel-base alloy coefficient of friction data lack clear mathematical bases and often pose some challenges to implement in FEA studies^{34, 36, 71}. The modified-Coulomb's friction law^{46, 54, 72} has been implemented in the current study, as will be discussed extensively in subsequent sections.

Previous process parameter simulations of LFW of Inconel 718 nickel-base superalloy have focused on heat transfer and deformation of weld^{44, 50, 52, 53}, however to date, a systematically derived and visible process window has not been published, to the best of the author's knowledge. Thus, the motivation for this work is the production of such an industry suitable process window guide for LFW for Inconel 718 nickel-based superalloy. Moreover, this work seeks to correlate the finite element thermomechanical modelling

results of the temperature and stress profile of the weld to the mechanical and microstructural properties of the weld, thus informing a process-structure-property framework for LFW.

These two objectives were achieved by developing a fully coupled 3D thermo-mechanical model of the LFW process for Inconel-718 nickel-based superalloy at the macroscale, and the model was implemented in a related computational simulation to predict systematically the influence of process parameters on the thermomechanical processes of the weld. This study will serve as valued input for the metallurgist, design and manufacturing engineers to configure accurately their process and equipment to achieve optimised material structure at the LFW joint.

2. Methods

In this paper, a fully coupled three dimensional (3D) thermomechanical LFW process computational model was developed in the general-purpose finite element solver Abaqus/Explicit (Dassault Systèmes, USA, 2017) ⁶¹. In the thermomechanical modelling, the two workpieces of the friction pair are both deformable. The workpiece dimensions for the FE model were sourced from the related publications to be used for verification of the FE modelling study ^{19, 32, 33}.

2.1 Material properties

Blisks are critical components of aero-engines and usually made from Inconel 718 (IN718) nickel-base alloy, known to exhibit excellent mechanical properties at elevated temperatures (~ 950 K) ^{1, 73}. Although readily used as a high-strength superalloy for the manufacture and repair of blisks, IN718 is an expensive and hard-to-machine alloy ^{74 75} and finds application in almost half of all aero-engines components ¹⁶. The material properties of IN718 used in this study are considered to be isotropic and homogeneous. These temperature-dependent material properties were sourced from a study by Qin et al.

⁵⁰. Table 1 summarizes the weight percentage chemical composition of Inconel-718 superalloy material ⁷⁵.

Table 1. Weight percentage chemical composition of wrought nickel-base superalloy Inconel 718

75

Cr	Mo	Nb	Al	Ti	Fe	C	Ni
19	3	5.1	0.5	0.9	18.5	0.04	52.96

Thermophysical properties of IN-718 ^{34, 50} are presented in Fig. 2. Additional material properties and LFW input process parameters are presented in Table 2.

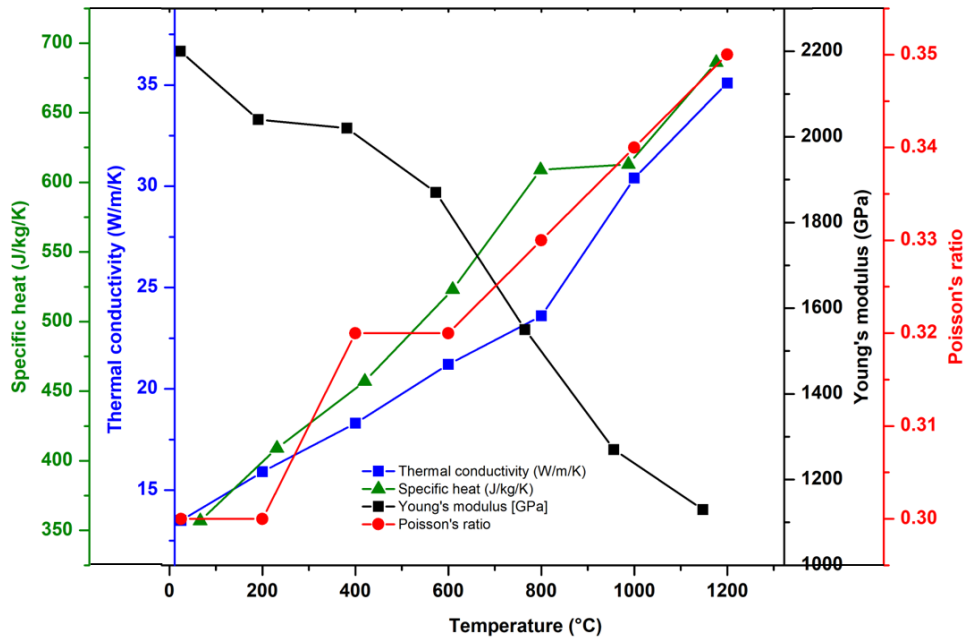


Figure 2. Temperature-dependent material properties of Inconel-718 nickel-based superalloy ⁵⁰.

71, 76

Table 2. LFW input process parameters for FEM study

Input parameter		Contact condition	
<i>Material properties</i>		Heat partition coefficient	0.5
Density ρ (kg.m ⁻³)	8420	Friction energy tr. Into heat	0.9
Elastic Modulus E (GPa)	221	Mean friction coefficient	0.2 - 0.5
Poisson's ratio ν	0.3	Shear stress limit	70-100
Conductivity λ (W.m ⁻¹ . °C ⁻¹)	13.4	<i>Welding process parameter</i>	
Specific heat c_p (J.kg ⁻¹ . °C ⁻¹)	460	Oscillation amplitude A (mm)	2.5 - 3.5
Expansion α_w (m.m ⁻¹ . °C ⁻¹)	1.20E-05	Oscillation frequency f (Hz)	15 - 25
Inelastic heat fraction	0.9	Applied pressure P (MPa)	200 - 500
Melting temperature (°C)	1300	Burn-off length L (mm)	2.5 - 3.5

2.2 Heat transfer and mechanical behaviour

The LFW process simulated in this study comprises both thermal and mechanical behaviour components, described by the heat diffusion equation and the mechanical equilibrium equation, respectively. The temperature history is calculated using the heat diffusion equation. ^{46, 66, 77}

$$\rho C_p \frac{\partial T}{\partial t} = \nabla \cdot \lambda \nabla T + Q_{int} \quad (2)$$

where ρ is the material density, C_p is the specific heat, λ is the temperature-dependant thermal conductivity, T is the temperature, t is the time. Q_{int} is the internal power generation per unit volume, also described as the power density dissipated by plastic deformation q_{pl} in LFW and expressed by

$$q_{pl} = \eta \bar{\sigma} \dot{\epsilon}^{pl} \quad (3)$$

where η , $\bar{\sigma}$, and $\dot{\epsilon}^{pl}$ are the thermal efficiency of plastic deformation, effective stress, and effective strain rate, respectively: ^{44, 46, 66, 77}

The thermal efficiency of plastic deformation, η is usually specified as 0.9 or 0.95^{34, 46}. Inelastic heat fraction is defined as 0.9 and the thermal boundary condition is described as:

$$q = h_k(T_w - T_c) + h_s(T_w^4 - T_c^4) = h(T_w - T_c) \quad (4)$$

where q , h_k , h_s , and h are heat flux, convective heat transfer coefficient, radiative heat transfer coefficient, and total heat transfer coefficient, respectively. The temperature of the boundary and ambience are represented by T_w and T_c , respectively. Computational modelling calculation has often been simplified by setting the heat transfer coefficient to a fixed value of $100 \text{ Wm}^{-2} \text{ K}^{-1}$ ^{34, 48}. Radiation heat loss is neglected on the power density dissipated by plastic deformation during LFW. The initial condition at time $t = 0$ is expressed by:

$$T|_{t=0} = T_0(x, y, z) \quad (5)$$

where $T_0(x, y, z)$ is the initial temperature function. The initial (reference) temperature is defined as room temperature, $25 \text{ }^\circ\text{C}$. Temperature dependencies of these defined parameters were obtained from reports^{50, 52} as shown in Fig. 2. The fraction of heat energy dissipated is split equally between the contacting surfaces at the weld interface. It is assumed that 95% of plastic deformation work is dissipated to the workpieces in the form of heat, and the remaining 5% accounts for crystalline defects^{30, 34}.

Mechanical behaviour during LFW is governed by the equilibrium equations defined as:

$$\rho \frac{\partial^2 u}{\partial t^2} = \nabla(\sigma) + \rho F \quad (6)$$

where u is the material displacement vector, σ is the stress tensor, F is the body force vector per unit mass, and t is the time. The classic von Mises generalised model of the rate-dependent material is:

$$f(\sigma, \varphi) = \sigma_{eq} - \sigma_s(\bar{\varepsilon}^{pl}, \dot{\bar{\varepsilon}}^{pl}, T) = 0 \quad (7)$$

where σ_{eq} and σ_s are the effective stress and material yield stress, respectively. Strain hardening, strain rate hardening, and thermal softening are defined as ⁴⁴:

$$\theta_1 = \frac{\partial \sigma_s}{\partial \varepsilon^{pl}}, \quad \theta_2 = \frac{\partial \sigma_s}{\partial \dot{\varepsilon}^{pl}}, \quad \theta_3 = \frac{\partial \sigma_s}{\partial T} \quad (8)$$

Thermal elastoplastic behaviour is described as strain rate decomposed into three main components as follows:

$$\dot{\varepsilon} = \dot{\varepsilon}^{el} + \dot{\varepsilon}^{pl} + \dot{\varepsilon}^{th} \quad (9)$$

where $\dot{\varepsilon}^{el}$, $\dot{\varepsilon}^{pl}$, and $\dot{\varepsilon}^{th}$ are the elastic, plastic, and thermal strain rate tensors in the matrix material, respectively. To calculate the plastic strain rate, an inelastic flow rule at high temperature can be used, which is defined as:

$$\dot{\varepsilon}^{pl} = \dot{\lambda} \frac{3\sigma'}{2\sigma_{eq}} \quad (10)$$

where σ' , σ_{eq} , and $\dot{\lambda}$ represent the deviatoric stress tensor, equivalent stress, and scalar quantity for the plastic flow rate, respectively. σ_{eq} is denoted by the equation in terms of deviatoric stress tensor as follows ^{44, 78}:

$$\sigma_{eq} = \left(\frac{3}{2} \sigma' : \sigma' \right)^{1/2} \quad (11)$$

The equivalent plastic strain rate is denoted as:

$$\dot{\varepsilon}^{pl} = \frac{\partial \dot{\varepsilon}^{pl}}{\partial t} = \left(\frac{2}{3} \dot{\varepsilon}^{pl} : \dot{\varepsilon}^{pl} \right)^{1/2} \quad (12)$$

2.3 Friction model

In this paper, a plastic deformable friction pair is used for modelling friction behaviour, as illustrated in a schematic (see Fig. 3). Contact formulation between workpieces is defined as the ‘surface-to-surface explicit’ contact algorithm. The magnitude of contact pressure is unlimited and automatically computed during the welding simulation process. Normal contact interaction is defined as hard (explicit default). Penalty tangential workpiece interaction—responsible for transmission of shear stresses across the contact interface—is defined via the friction coefficient in the Abaqus/Explicit solver^{27, 44}.

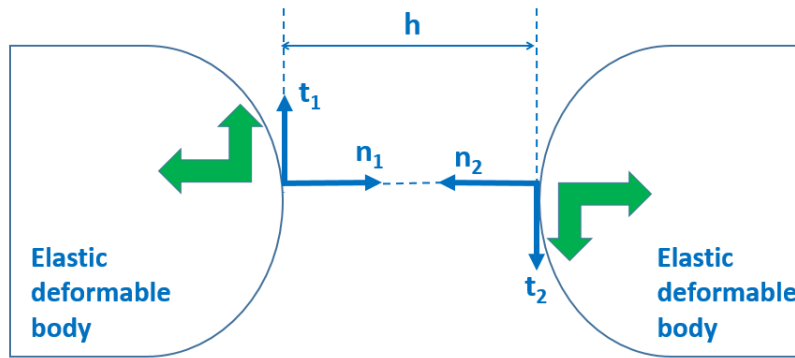


Figure 3. Schematic of the contact condition in a plastic deformable friction pair.

According to classic Coulomb’s law, a proportional relationship is defined between friction shear stress and normal contact pressure expressed as:

$$\tau_{fr} = \mu \sigma_n \frac{\Delta v_s}{|\Delta_s|} \quad (13)$$

where τ_{fr} is the friction shear stress, μ is the Coulomb’s coefficient of friction, and Δv_s is the relative sliding velocity between rubbing bodies. The basic Coulomb’s law has been widely used, with and without variable-dependencies, in LFW process modelling studies^{63, 64, 67-69, 79, 80}. The focus in all friction models is the determination of friction stress via

the friction coefficient. At low-stress levels, the classic Coulomb's law can reasonably estimate friction conditions. However, it is often unsuited for high-stress levels, overestimates the friction stress conditions, and especially where the coefficient of friction is defined as a constant value. Multiple studies have reported a quadratic relationship between friction coefficient and temperature in the computational modelling of plastic contact during LFW^{39, 49, 67, 69, 79, 80}. However, the friction coefficient depends on other measurable variables, such as sliding velocity and contact pressure, besides temperature. This variable dependence can be expressed as a function given by:

$$\mu = f(\sigma_n, v_s, T) \quad (14)$$

where σ_n is the contact pressure, v_s is the slip velocity, and T is the interface temperature between the contacting bodies. Although several mathematical relationships have been reported that consider different influencing parameters^{53, 64, 67, 72}, it is still a challenge to derive a simple mathematical equation that properly expresses all influencing factors contributing to high strain rates, high tangential velocities, strain, and increasing temperature during LFW. In this study, a mathematical relationship specifically derived from IN718 friction and wear experiments by Geng et al.⁷², is expressed as an exponential function. It is a modified Coulomb's friction law that closely replicates the variable dependencies expressed as:

$$\mu = a\sigma_n^b T^c \exp(dv_s) \quad (15)$$

where the constants $a, b, c, \text{ and } d$ are specified as 0.12, -0.233, 0.471, and -0.739, respectively⁷². The user-subroutine VFRIC was implemented for a variable-dependant modified-Coulomb friction law, as suggested by Maalekian et al.⁴⁶ for steel and Geng et al.⁵² for IN718 superalloy. Fig. 4 indicates the coefficient of friction values that have been calculated for the current study, following the already described modified-Coulomb's friction law.

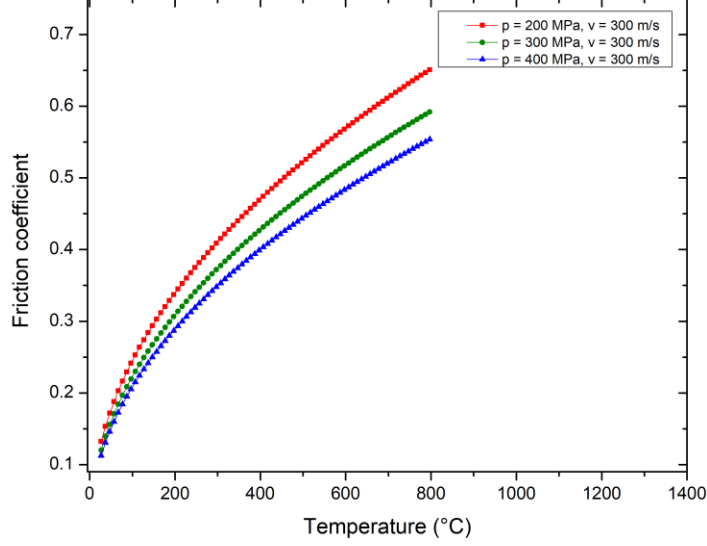


Figure 4. Friction coefficient curves for different values of sliding velocity, normal contact pressure, and interface temperature

2.4 Constitutive material model for IN718 alloy

In this paper, an up-to-date constitutive material model was specified for the FE modelling of LFW of IN718 superalloy^{44, 50, 52-54}. The elastic response of the material is assumed to be governed by Hooke's Law. Eqns. 16 and 17 denote the Strain-compensated Arrhenius equation for the plastic material behaviour of Inconel 718 alloy during LFW process^{44, 50, 52-54}.

$$\sigma_y = \frac{1}{\alpha(\varepsilon)} \ln \left\{ \frac{Z(\varepsilon)^{1/n(\varepsilon)}}{A(\varepsilon)} + \left[\left[\frac{Z(\varepsilon)^{1/n(\varepsilon)}}{A(\varepsilon)} + 1 \right]^{2/n(\varepsilon)} + 1 \right]^{1/2} \right\} \quad (16)$$

$$Z(\varepsilon) = \dot{\varepsilon} \exp \left[\frac{Q(\varepsilon)}{RT} \right] \quad (17)$$

where σ_y is the yield flow stress, $\dot{\varepsilon}$ is the strain rate, T is the absolute temperature, R is the universal gas constant. $Q(\varepsilon)$ is the deformation activation energy, $\alpha(\varepsilon)$, $n(\varepsilon)$, and $A(\varepsilon)$

are material constants. They are respectively expressed as polynomial functions of deformation strain as:

$$\begin{aligned}
 A(\varepsilon) &= B_0 + B_1\varepsilon + B_2\varepsilon^2 + B_3\varepsilon^3 + B_4\varepsilon^4 \\
 n(\varepsilon) &= C_0 + C_1\varepsilon + C_2\varepsilon^2 + C_3\varepsilon^3 + C_4\varepsilon^4 \\
 Q(\varepsilon) &= D_0 + D_1\varepsilon + D_2\varepsilon^2 + D_3\varepsilon^3 + D_4\varepsilon^4 \\
 \ln A(\varepsilon) &= F_0 + F_1\varepsilon + F_2\varepsilon^2 + F_3\varepsilon^3 + F_4\varepsilon^4
 \end{aligned}
 \tag{18}$$

The coefficients of polynomial functions for the alloy material can be found in the study by Geng et al.⁵².

2.5 FE modelling method

The fully coupled thermo-mechanical model was implemented using the commercially available finite element software package Abaqus. Abaqus/Explicit solver has the capability for complex contact formulation and dynamic remeshing that are required in high-strain deformation thermomechanical analyses.

Multiple published articles have developed either 2D^{6, 34, 80} or 3D^{54, 81} models with one deformable and one rigid workpiece. Using such an approach only provides partial insight into the thermomechanical analysis because weld deformation does not occur on the rigid workpiece. Most published LFW process finite element models are for one rigid body and one deformable-body for the LFW process, and few computational models have been developed recently in 2D^{66, 71} or 3D^{44, 50, 52, 53} for two deformable bodies. This research presents a 3D FE model that captures friction-contact formulation for two deformable workpieces rubbing against each other during the LFW process. This treatment of two workpieces as deformable bodies depicts a complete thermomechanical interaction and provides useful information on the weld deformation mechanism.

2.5.1 Setup of computational modelling

In the current numerical simulation, the two workpieces—the top workpiece for the disk and the bottom workpiece for the blade—were discretized using the deformable plane strain formulation. Both deformable workpiece billets, as shown in Fig. 5, have dimensions of 33 mm by 14 mm by 13 mm. They are adjacent to each other and there is an initial contact at the intended weld interface. Element type C3D8RT (8-node thermally coupled brick, trilinear displacement and temperature, reduced integration, hourglass control) was specified. The thermomechanical modelling for the LFW process lasts for 5.0 s of total welding time.

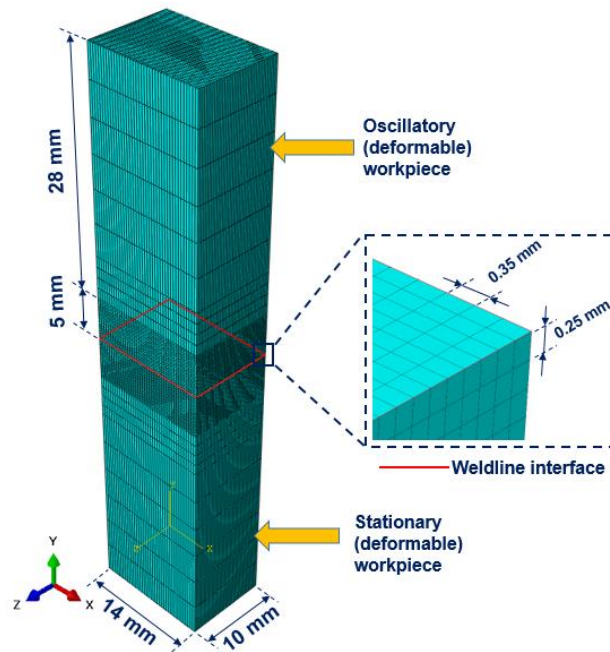


Figure 5. 3D fully coupled thermomechanical LFW model with friction-paired deformable workpieces

The same multi-partition meshing strategy has been applied to both workpieces. There are 26184 elements and 28442 nodes for the entire model. Mesh refinement is specifically directed along the friction interface and region where extreme friction contact and high gradients of solution variables—temperature and displacement—are observed. Biased

seeding is defined on the edges of the specimen at the regions closest to the weld line interface.

2.5.2 Initial and boundary conditions

Mechanical boundary conditions are defined on the top workpiece as friction pressure and sinusoidal displacement, and on the bottom workpiece as a fixed constraint (see Fig. 5). The displacement is controlled by a sinusoidal relation:

$$x = A \sin 2\pi ft \quad (19)$$

where A is the amplitude of oscillation (mm), f is the frequency of oscillation (Hz), and t is the instantaneous weld time, from 0 to 5.0 s. The workpieces are clamped in position, starting at a distance (y-axis) of 10 mm away from the weld interface.

2.5.3 Numerical solution algorithm and mesh convergence analysis

During the computational modelling of the friction welding process, large strain values are obtained, which result in excessive distortion of the computational mesh, particularly in 3D computational modelling. The arbitrary Lagrangian-Eulerian (ALE) adaptive meshing is implemented for automatic solution mapping, which controls excessive element distortion^{61, 82}. Mass-scaling algorithm was formulated at every analysis step in the Abaqus/Explicit solver. The quasi-static process modelling involves a large number of time increments in the regular time scale. To ensure reasonable computational cost, a constant value of 800 was specified as the semi-automatic mass scaling objective definition at the beginning of each analysis step^{61, 82}. The kinematic energy should typically be less than 5% of the internal energy⁸³. This criterion for defining a suitable mass scaling factor has been used extensively in multiple numerical studies to achieve reasonable stability and accuracy of the numerical procedure^{27, 52, 53}.

Refined mesh size of length 0.3 mm was specified at the partitioned region 5 mm from the weld interface. High temperature and plastic deformation usually occur around this region of the computational mesh domain. A coarsened mesh size of length 2.3 mm was specified

in the region (partition) that is 10 mm away from the weld interface. For the partitioned region within 5 mm from the weldline interface, the calculated maximum temperature is insensitive to using lower element size, especially when the element length is reduced below 0.6 mm. This computational domain discretisation is based on a mesh sensitivity study (see Fig. 6) that shows the effect of reducing the mesh size (same as increasing the number of elements) and the resultant maximum temperature calculated during the computational modelling. The mesh sensitivity analysis was conducted with the welding process parameters for setup J6 where friction pressure is 400 MPa, oscillation amplitude is 2.9 mm, and oscillation frequency is 25 Hz (as shown in Table 3).

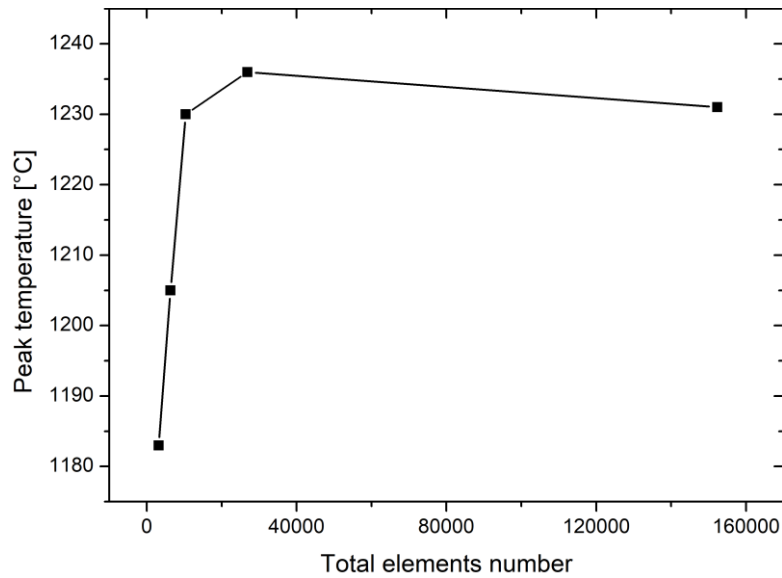


Figure 6. Mesh convergence analysis conducted for the FE modelling study

3. Results and discussion

Table 3 presents a summary of the key LFW process parameters that were employed in the ten different setups (from setup J1 to setup J10) of the research. In the ten different configurations of LFW, the normal pressure p_f , the friction amplitude A_0 , and the friction frequency f_0 vary.

Table 3. Parameters applied during the LFW process simulations

# FEM	Friction pressure p_f (MPa)	Friction frequency f_0 (Hz)	Friction amplitude A_0 (mm)	Q_{SPI} (kW.m ⁻²)
J1	200	15	2.5	1193.7
J2	200	25	2.9	2307.7
J3	200	25	3.5	2785.2
J4	300	25	2.9	3461.6
J5	300	25	3.5	4177.8
J6	400	25	2.9	4615.5
J7	400	25	3.5	5570.4
J8	400	30	2.9	5538.6
J9	500	15	2.5	2984.2
J10	500	25	2.9	5769.4

3.1 Thermal history and deformation of the workpiece

Temperature uniformity at contact interface and the value of maximum interface temperature are pertinent factors that affect the quality of the weld joints in terms of such as appropriate material microstructure and optimal mechanical properties. The contour plots in Fig. 7 show the temperature fields of the bottom workpiece for a welding setup J6 at various welding times during the LFW process. The three curves in Fig. 7 depict the temporal evolution of the bottom workpiece at three different positions on the friction interface (shown as white coloured nodes). All three curves show a periodic fluctuation of temperature with time during LFW. Position A is a node located at the mid-region of the bottom workpiece interface, which records the highest temperature history. Position B is a node located at 2 mm from position A, with the second-highest temperature history. Position C is a node located 4 mm away from position A and indicates the least temperature history. Node A at the mid-region is always within contacting workpiece surfaces at the interface throughout the LFW time. However, there is periodic non-contact of nodes B and C between the interface of the two workpieces during the LFW process simulation. This happens because of the oscillation of the top workpiece relative to the bottom workpiece. The time of non-contact for node C is more significant than for node B at 3.0 s of LFW time when flash formation has started. This intermittent non-contact of nodes B and C (on

the interface of the bottom workpiece) to the interface of top workpiece continues until the completion of LFW at 5.0 s of total welding time.

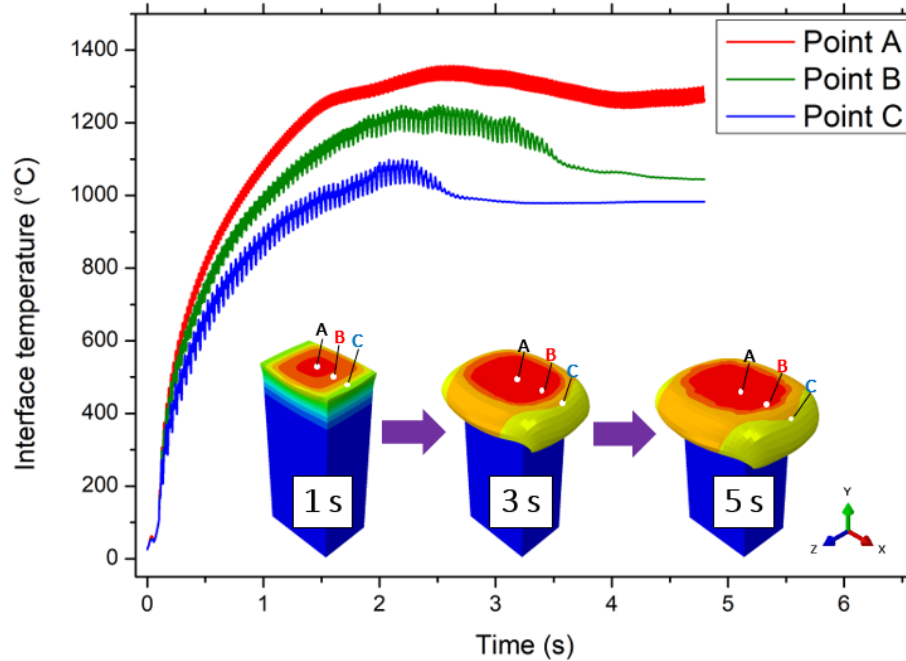


Figure 7. Temporal evolution of the maximum temperature of one workpiece during the LFW process at different locations on the friction interface and different LFW time, for setup J6.

At the start of LFW process, the mid-region of the weldline interface experiences rapid temperature rise to 1000 °C within 1.0 s of welding time because of the generation of friction heat. There is heat transfer from the weld interface to the rest of the workpiece because of conduction. Subsequently, the weld joint periphery and material bulk steadily increase in temperature as the LFW process progresses. At a weld time of 1.0 s, the maximum temperature at the centre of the friction interface is 1022 °C. The mid-region of the workpiece where maximum temperature is predominantly located is seen to be narrow, indicating that there is a large temperature gradient near the interface. However, the peripheral edges have a temperature of 606 °C due to periodic loss of contact between the rubbing surfaces. Other factors contributing to considerable temperature difference—between the interface central region and periphery—are the direction of reciprocation,

reciprocating displacement, and convective heat loss. There is no flash formation observed at a weld time of 1.0 s.

At a weld time of 3 s, plastic work is significant and forming flash at the weld interface (as shown in Fig. 7). Following the rapid increase in temperature is plastic deformation at the interface; softened material is extruded near the friction interface by rubbing workpieces under high compressive force. Flash is formed around the interface in the direction of reciprocation. As the LFW progresses from 3.0 s to 5.0 s, the formation of flash becomes increasingly significant, which is characteristic of the quasi-steady state of the friction (transition) phase during the LFW process. The maximum temperature of the workpiece reaches 1298 °C, at weld completion time of 5.0 s, which is well below the liquidus temperature of Inconel-718 superalloy (1360 °C). At no time during the welding process was the temperature observed to rise beyond the liquidus temperature of IN-718 superalloy (~ 1360 °C).

Fig. 8 shows the heat flux distribution of the weld joint at different LFW process times for setup J6. As the workpieces contact each other under high compressive force, heat is initially generated at the mid-region of the joint interface within a short time of less than 1.0 s, resulting in a rapid increase in weld interface temperature.

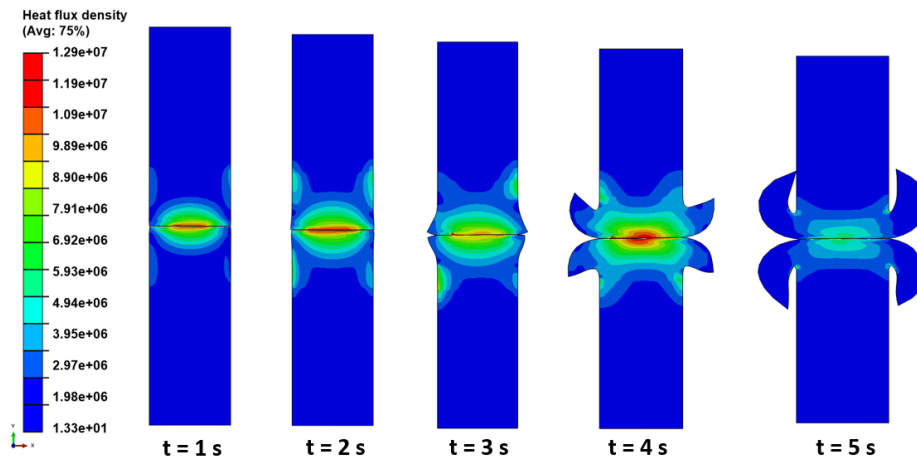


Figure 8. Evolution of heat flux density at the weld joint for different LFW times for setup J6 where $p_f = 400 \text{ MPa}$, $f_0 = 25 \text{ Hz}$ and $A_0 = 2.9 \text{ mm}$.

At 1.0 s of total welding time, the maximum heat flux is calculated as 9.21 MW/m^2 . During this initial/conditioning phase of the LFW process, the mainspring for heat generation is

friction work. The two workpieces are frequently out of alignment (y-axis direction); thus, minimum heat flux is calculated at the highest displacement (2.9 mm) of the oscillating top workpiece and maximum heat flux is calculated at lowest displacement (0 mm) of the oscillating top workpiece relative to the stationary bottom workpiece. Beyond 1.0 s of welding time, heat flux distribution is no longer concentrated at the mid-region of the interface. Further increase in heat flux density is observed as a non-uniform field distribution at the interior of the workpiece material and around non-central portions of the weld interface. This results in inhomogeneous temperature field distribution at the weld interface.

Between 1.0 s and 3.0 s of total welding time, the equilibrium welding phase is fully underway as heat generation continues. The maximum heat flux is constantly changing between 16.3 to 22.4 MW/m². Within the welding time of 3.0 s to 5.0 s, the maximum heat flux at the mid-region of the LFW joint interface has reduced from 12.9 to 5.93 MW/m². In a study by Geng et al.⁵², the average effective heat flux was calculated within the range of 5.4 to 5.6 MW/m² during the quasi-steady-state welding of IN718 superalloy. This range of values is consistent with the heat flux calculated in the current paper for LFW time of 4.0 s to 5.0 s. The periphery of the workpiece and extruded flash show the lowest value of heat flux density at 1.98 MW/m². Heat conduction and heat convection mechanisms drive heat flow distribution from the weld interface to the periphery of both workpieces and away from the weldline interface^{30,44,69}. An increase (or decrease) in heat flux field distribution will result in an increase (or decrease) in the interfacial temperature of the deforming workpieces during LFW. Computational modelling results of heat flux density show that it has a periodic characteristic and is often inhomogeneous around the interface of the weld joint during LFW.

3.2 Flash formation and axial shortening

LFW is accompanied by material extrusion or flash formation. Flash is formed when material that was previously at the weld interface is heated, softened, and expelled in the direction of oscillation during friction welding^{13,84}. Flash formation is beneficial for the expulsion of oxides and contaminants, and the creation of atomically clean weld joint with high bonding affinity^{1,2,8}. Fig. 9 shows cross-section view cuts along the y-axis, revealing

the local temperature evolution and formation of flash during the LFW of Inconel-718 alloy. The process parameters of LFW are based on setup J6, as presented in Table 3.

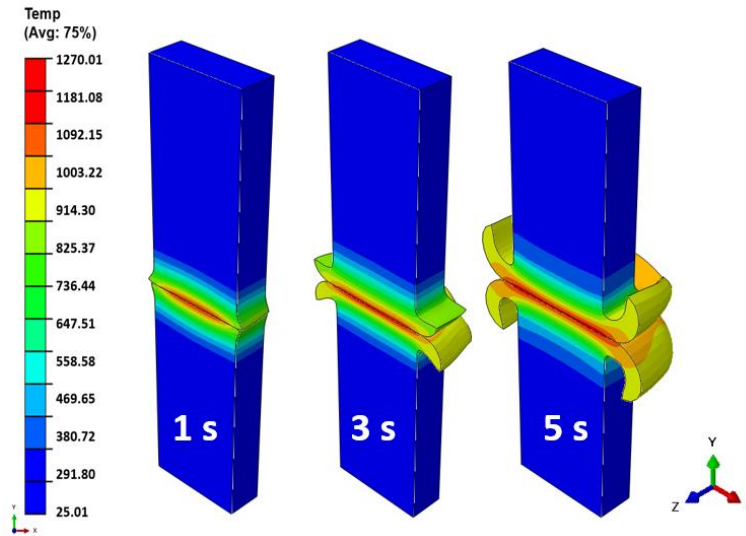


Figure 9. Evolution of the flash of the weld during the LFW process. The contour plots represent local interface temperature at different LFW times for setup J6

Local interface temperature contour plots of the workpieces are shown for flash formation at different LFW times. At 1.0 s of welding time, the oscillating and stationary workpieces show similar temperature fields at the friction interface (1003.22 °C). At 2.0 s of welding time, the material at the friction interface is sufficiently softened and flash formation has started for both workpieces. However, the temperature of formed flash material for the oscillating workpiece (825.37 °C) is relatively lower than the temperature of formed flash material on the stationary workpiece (914.30 °C). This temperature difference is more obvious at 5.0 s of welding time when the flash temperature of the oscillating workpiece is 914.30 °C while that of the stationary workpiece is 1003.22 °C.

Another difference is that formed flash is extruded up to a length of 4.5 mm for the oscillating workpiece and 4.65 mm for the stationary workpiece at 5 s when LFW has completed. This extruded flash material length is also referred to as the burn-off length. The difference in burn-off length calculated for both workpieces can be attributed to the variation in mechanical constraints, whereby the top workpiece is oscillating rapidly only in the x-axis direction, while the bottom workpiece is stationary and allowed to travel only

in the y-axis direction under friction pressure. There is no plastic deformation occurring on the regions that are at a distance of 10 mm away from the interface on both workpieces throughout the LFW process.

As the metal layer softens and gets expelled at the friction interface, the workpiece reduces in height, which is referred to as axial shortening. Axial shortening (or mechanical upset) is a measure of the difference in axial workpiece dimension (y-axis) before starting and after completing the LFW process. During welding, the axial shortening, just like flash formation, increases with welding time. The experimentally measured result for total axial shortening is (4.8 ± 0.2) mm for setup J6 according to Geng et al.'s study⁴⁴. By FEA calculated axial shortening in the current study, the total shortening length was approximately 5.9 mm. Geng et al.³² recommended that axial shortening must be greater than 4.8 mm to achieve a sound IN718 weld joint manufactured free of oxides at the interface. The FEA results of flash formation and axial shortening are pertinent because of their role in understanding the plastic deformation mechanism and the determination of optimal LFW process parameters.

3.3 Stress/strain distribution

The FEA results presented herein are based on the LFW configuration J6. Figs. 10 and 11 show the contour plots for the von Mises stress and equivalent plastic strain fields, respectively, at different LFW time.

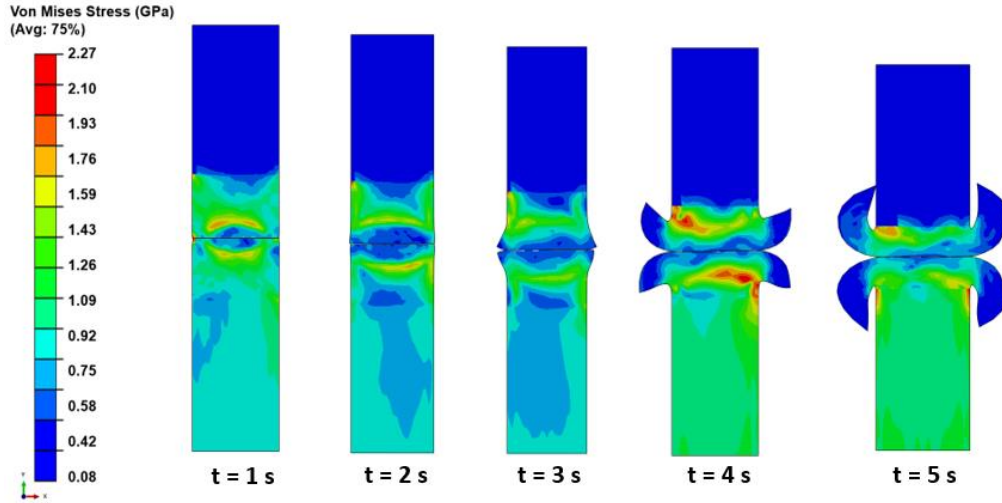


Figure 10. Evolution of von Mises stress at the weld joint for different welding times for LFW setup J6.

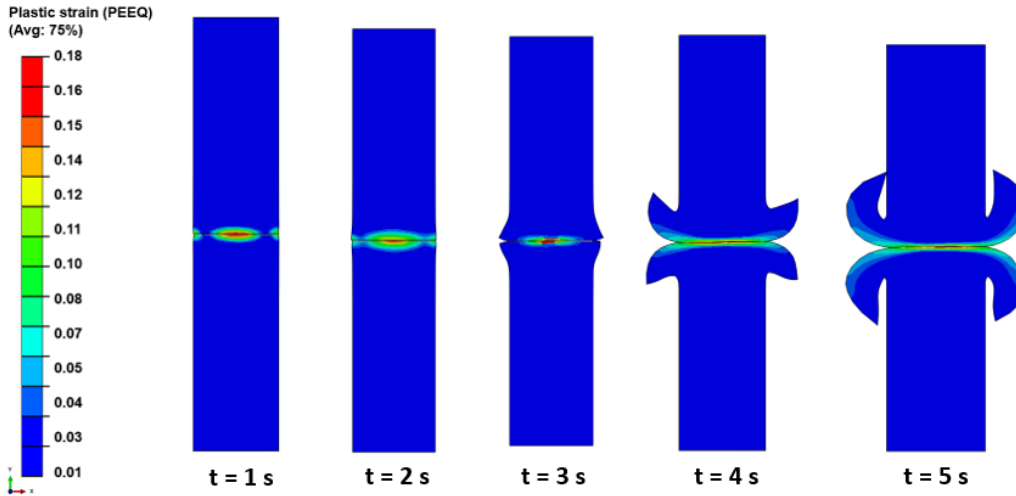


Figure 11. Evolution of equivalent plastic strain (PEEQ) at the weld joint for different welding times for LFW setup J6.

Similar to the publications by Yang et al.³⁴ and Geng et al.⁴⁴, the variation of maximum Mises stress is investigated by using a plane strain model. Masoumi et al.³³ noted that the exact determination of strain at the weld interface is difficult to achieve experimentally due to the dynamic nature of the LFW process. There is a continuous variation of the location of maximum Mises stress and maximum plastic strain on both workpieces from the start to

completion of LFW. At 1.0 s of welding time (initial phase of LFW) the von Mises stress and plastic strain fields of the oscillating workpiece are the same for the stationary workpiece. The maximum value of equivalent stress is 1.93 GPa at the peripheral edges and the equivalent plastic strain at the interface is 0.15 for the two rapidly rubbing workpieces. However, the values of stress and strain fields—at 10 mm distance from the friction interface—are different between the oscillating and stationary workpieces.

Between the transition phase and equilibrium phase of LFW (up to 3.0 s of welding time), the maximum Mises stress reduced to 0.42 GPa on the friction interface, while the maximum plastic strain has increased to 0.16. Yang et al.³⁴ and Qin et al.⁵⁰ have described the decrease in maximum stress during LFW as the quasi-steady-state behaviour of IN718, where more increase in the temperature field at the friction interface only reduces the Mises stress field.

During the equilibrium phase of LFW (3.0 s to 5.0 s), the von Mises stress field decreases at the friction interface with time (where there is high-temperature gradient) and increases with time on the peripheral edges (where there is low temperature). However, the plastic strain continues to increase at the friction interface (0.18) and indicates much lower values at the peripheral edges (0.07) and on the formed flash material (0.05). The deceleration phase of welding (4.0 s to 5.0 s of welding) shows a maximum plastic strain field on the friction interface compared to the peripheral edges. From 1.0 s to 5.0 s of LFW process time, there is zero Mises stress and plastic strain distribution in the interior and boundaries of each workpiece at 20 mm distance from the friction interface.

Variations in stress and strain field distributions are attributed to several factors. First, the different mechanical constraints imposed on the interacting workpieces. Second, the periodicity of displacement for two workpieces that are rapidly rubbing against each other under large compressive force. Third, the progressive shortening of workpieces when softened material is extruded as flash in the direction of reciprocation. The combined effect of rubbing surface condition and applied friction pressure leads to compression and shear deformation, as reported in multiple studies^{44, 50, 52, 53}. Both dominant types of deformation influence the distribution of von Mises stress and equivalent plastic strain of the IN718 linear friction welded joint. The FEA results have shown that throughout the LFW time,

the Mises stress field is constantly changing all on the workpieces while the equivalent plastic strain is uniformly increasing on the interface and at the peripheral edges.

3.4 Optimisation of welding input process parameters

In this section, the interface temperature history results of the FE model are presented and discussed for different welding input process parameters. Fig. 12 shows a comparison of temperature field at 5.0 s of welding based on different LFW configurations (see Table 3). Fig. 13 shows the calculated peak temperature at the centre of the friction interface of the bottom workpiece for six simulated weld joints. Setup J2 and J3 do not show any flash formation.

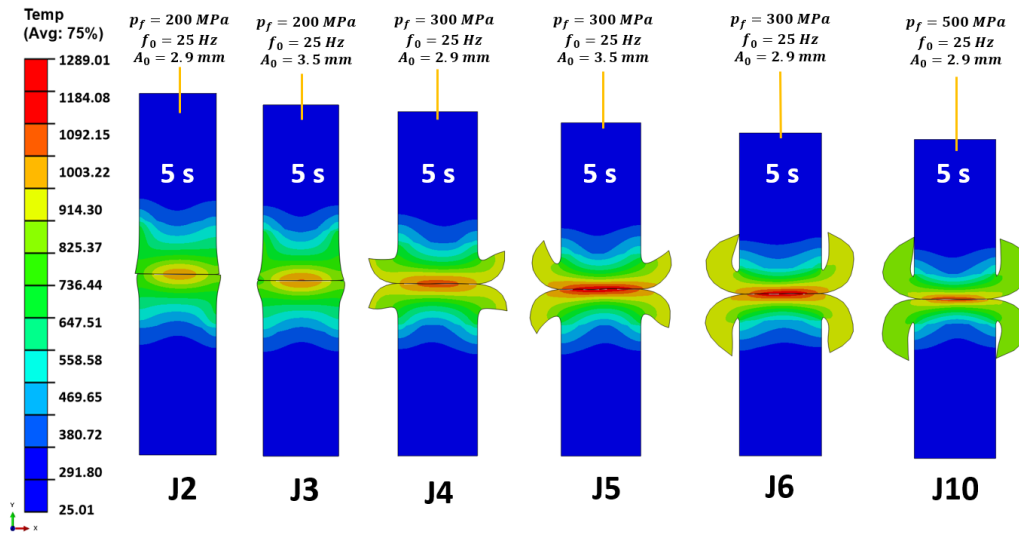


Figure 12. Comparison of temperature at the weld interface for six simulated joint setups (J2, J3, J4, J5, J6, and J10). LFW process parameters of all six joint setups are summarised in Table 3.

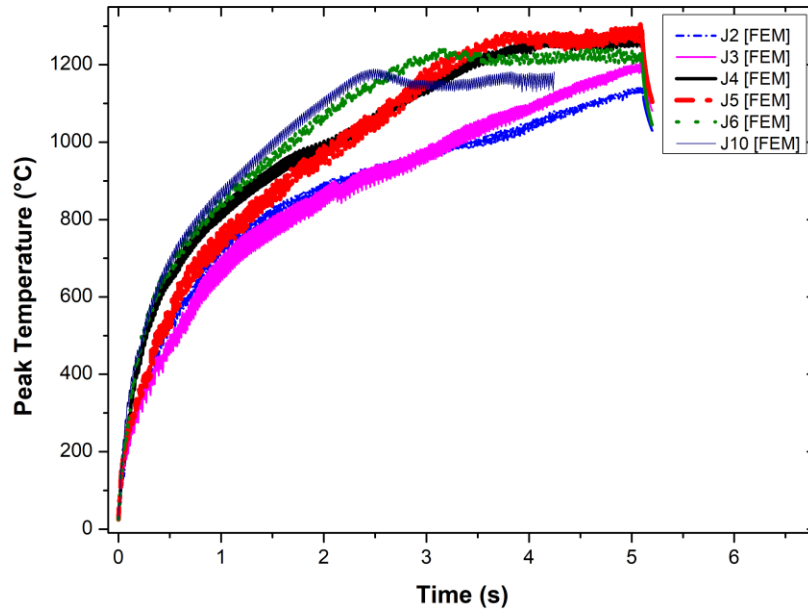


Figure 13. Comparison of peak temperature of a node located at the mid-region of the bottom workpiece for six simulated weld joint setups (J2, J3, J4, J5, J6, J8, and J10) (see input welding process parameters in Table 3).

Setup J4 shows that flash is formed but not significantly extruded at the peripheral edges. There is clear flash formation for setups J5, J6, and J10, where the flash size increases accordingly due to the specified welding process parameters. Setups J4 and J5 have axial shortening values less than 5 mm while setups J6 and J10 have axial shortening values greater than 5 mm. Geng et al. measured the axial shortening of joint setups J2, J3, J4, J6 and J10 as 1.6 ± 0.2 , 2.3 ± 0.3 , 4.8 ± 0.2 , 5.1 ± 0.3 , and 6.8 ± 0.4 mm, respectively. This is in reasonable agreement with the computational modelling results where J4, J5, and J6 have a range of axial shortening values between 2.5 mm and 7 mm.

Fig. 13 indicates that higher temperature values were predicted at the weld interface for setup J5 than J4 because the oscillating amplitude was increased from 2.9 mm to 3.5 mm. The least specific power input value was calculated as 1.06 MW/m^2 for setup J2 where heat generation is insufficient and the calculated maximum interface temperature is the lowest at $886 \text{ }^\circ\text{C}$ compared to the other five setups, thus, resulting to only partial softening of the rubbing surfaces without formation of flash shape. There is no significant joint formed between the rubbing surfaces. The highest specific input value (9.89 MW/m^2) was recorded

for setup J10 that has a peak interface temperature of 1289 °C, with formation of curly flash at the end of the LFW process simulation.

The overall results of the optimal welds were simulated for welding conditions ($p_n = 200$ to 500 MPa, $A_0 = 2.9$ mm, and $f_0 = 25$ Hz). Averaged peak temperature values were calculated for the optimal welds as approximately 1240 °C. All phases of the friction welding process were attained, and curly flash was formed, with the most flash formed for the highest friction pressure of 500 MPa. The optimal input process parameters resulted in maximum temperature values below the liquidus melting point temperature of IN718 (~1360 °C); an important attribute of a sound weld with excellent mechanical properties. This is because the metal alloy begins to plasticise at temperatures where no undesirable microstructures are created. Anderson et al.⁸⁵ and Masoumi et al.²⁸ have affirmed that the gamma double prime (γ'') precipitate can morph to deleterious delta (δ) phase when subjected to elevated temperature beyond its dissolution temperature. Indeed, optimal LFW process conditions are desirable to avoid the formation of brittle intermetallic phases. LFW is a rapid metal alloy joining process and the resultant microstructure within a few seconds of joining two components could set the tone for the behaviour of the welded component—blisks for instance—when under severe and complex operational conditions.

3.5 Identification of LFW process window

So far, the premise for assessing the LFW process window has been established. The results of such as temperature field distribution, stress field, strain field, and heat flux field have been discussed in relation to evolving microstructural and mechanical properties. The LFW process window is herein represented as a 3D plot of the data points determined by 10 different combinations of key LFW process parameters of such as frequency, amplitude, and friction pressure. The process window shows that for multiple combinations of input welding parameters, the resultant weld temperature and heat flux field can be described as either optimal or sub-optimal configurations (see Fig. 14).

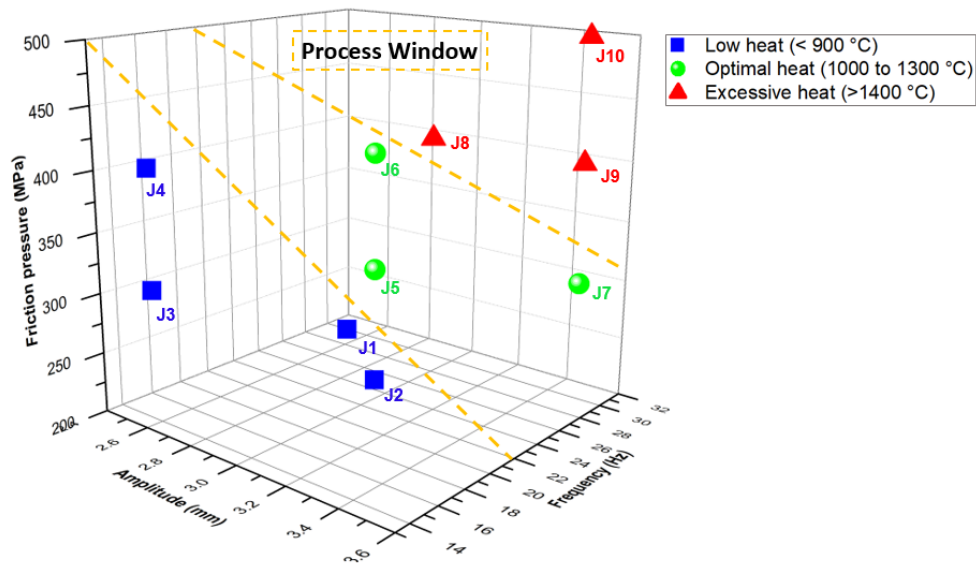


Figure 14. Maximum temperature-based LFW process window for ten simulated weld joint setups (J1 to J10). The 3D plot shows the limits for the optimal and sub-optimal specification of the weld processing parameters of such as frequency, amplitude and friction pressure.

The setups for optimal input welding process parameters have so far been discussed. They can be identified on the process window as green circles. Sub-optimal results were attained in setups J1, J2, J3, J4, J8, J9, and J10 because of the inadequate or over-specified combination of welding process parameters. They are identified as blue squares (J1, J2, J3, and J4) and red triangles (J8, J9, and J10) on the LFW process window. J1 and J2 setups resulted in less than 1000 °C maximum temperature at the weld interface. The low specification of the input LFW process parameters did not lead to bonding or flash formation because enough heat flux field was not generated. J8 and J9 setups are over-specified configurations that led to excessive heat generation at the weld interface. There was over-prediction of the interface temperature, which exceeded the liquidus temperature of IN718 (~ 1360 °C) and introduced occasional numerical convergence difficulty. Further, over-predicted weld temperature was accompanied by excessive prediction of friction stress that by far exceeded the shear flow stress of the material, leading to distortion of the computational mesh domain.

So far, three setups (J5, J6, and J7) have been categorised as the optimal results within the LFW process window. They are primarily identified as configurations whose maximum interface temperature was above the solidus temperature (1250 °C) and below the liquidus temperature (1360 °C) of IN718 alloy. The maximum interface temperature of setups J5, J6, and J7 were calculated as 1250 °C, 1265 °C, and 1280 °C, respectively. In addition, these setups produced a curly flash shape and axial shortening length between 4.8 mm and 7 mm, which is within the recommended critical axial shortening length in study ⁴⁴. The optimal setups also indicate that the input process parameters are within the following range: oscillation amplitude (2.5 mm to 3.5 mm), oscillation frequency (20 to 30 Hz) and corresponding friction pressure (300 MPa to 500 MPa). Below these identified ranges, the plasticised material at the weldline interface cannot progress to the extrusion of thermoplastic material at the periphery of workpieces. Also, above this optimal input welding parameter range, excessive flash is formed for a stable computation while sometimes, numerical instability could result because of excessive distortion of the computational domain mesh.

3.6 FE model verification

The computational-analysis results obtained from the current numerical procedure have been verified by measured data published in studies ^{32, 50}, considering that these LFW experiments utilised the Inconel-718 superalloy material and the same input welding process parameters for setup J6 (see Table 3).

3.6.1 Validation of temperature history

The temperature field results of LFW—for a node located at 5.0 mm away from the weld interface—were validated by Geng et al.’s experimentally measured thermal histories, for a thermocouple positioned at 5.0 mm distance from weld interface ⁴⁴. Both sets of thermal histories (for four setups, which are J2, J4, J6, and J8) depict a highly similar trend in the temperature evolution at the specified position (see Fig. 15). As the LFW input process parameters increase from setups J2 to J10, there is a corresponding increase in temperature histories as shown in Fig. 15. The strong correlation between FE modelling results and

experimentally measured thermal histories demonstrates the reliability of the computational model.

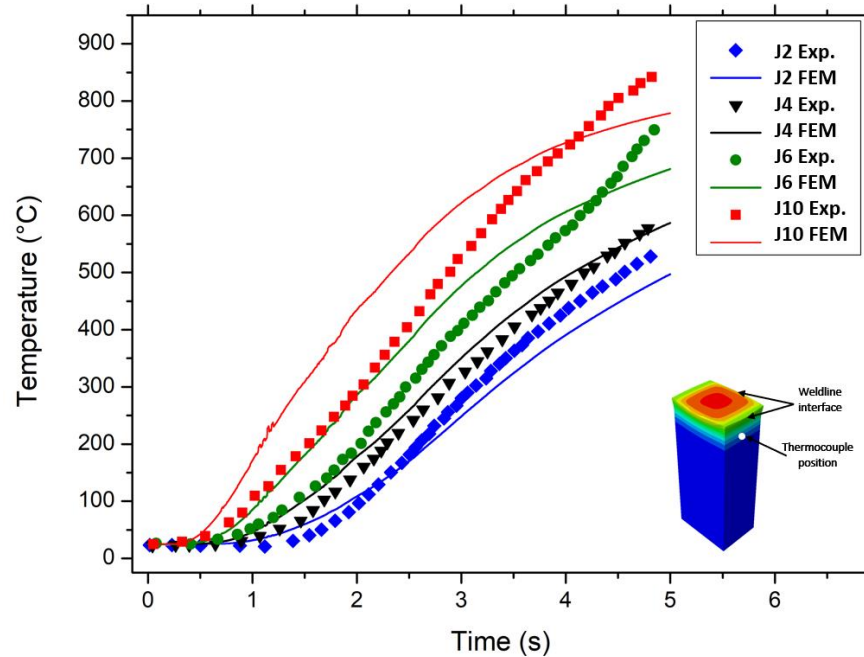


Figure 15. Comparison of experimentally measured data (Exp.) and simulated (FEM) temperature history ⁴⁴.

3.6.2 Qualitative comparison of flash formation and axial shortening

Flash morphology from current paper FEA has been compared to experimentally measured macrostructural shape and high-speed camera images reported in Geng et al. ⁴⁴ for the setup J6 input welding process parameters (see Fig. 16). The contour plots in Fig.16 show the temperature fields of the weld during LFW. At different welding time (1.0 s, 3.0 s, and 5.0 s), the progression of flash formation is presented, where the size of the formed flash increases simultaneously with the decreasing axial length of workpieces.

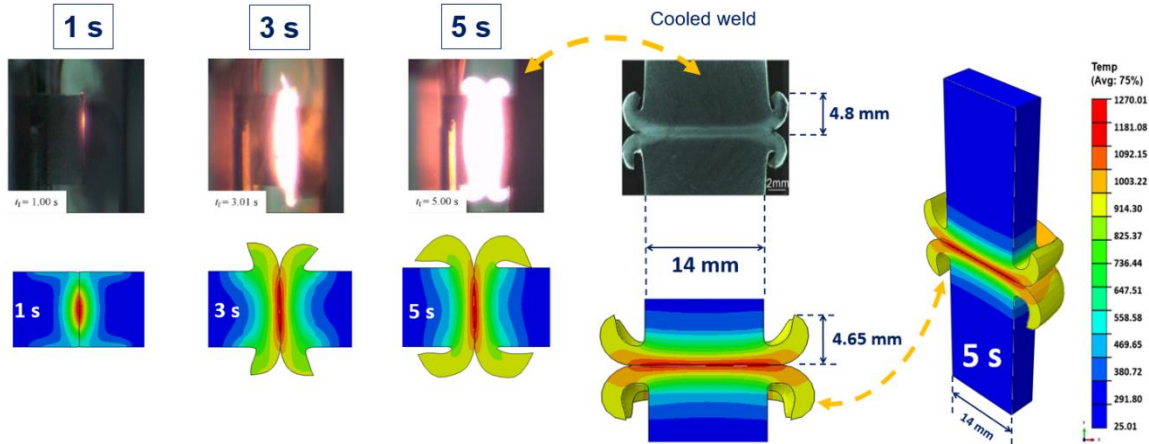


Figure 16. Flash morphology comparison of current research to experimental work by Geng et al. The welding parameters used are: $p_n = 400 \text{ MPa}$, $A_0 = 2.9 \text{ mm}$, and $f_0 = 25 \text{ Hz}$ ⁴⁴

Between 1.0 s and 5.0 s of welding time, for the computational modelling results, the temperature field on the flash shape has increased from 558.58 °C to 1003.22 °C. This is concurrently accompanied by increasing flash size and burn-off length up to 4.5 mm for the oscillating workpiece and 4.65 mm for the stationary workpiece. Because there is no temperature measurement scale presented in the referenced experimental LFW publication by Geng et al.^{32, 44}, only the cooled macrostructure shape of flash is compared at 5.0 s of welding completion.

The flash formation obtained by computational modelling in this paper showed high-level similarity to the experimentally derived results by Geng et al.³² more so that both studies used the same J6 configuration. Geng et al.⁴⁴ argued that the burn-off length for setup J6 should ideally correspond to an axial shortening length of 5.0 mm. The FEA results of the current paper show a burn-off length of 4.65 mm. However, the computational modelling results of flash formation in the current paper did not agree with the results reported in Yang et al.³⁴ for the IN718 alloy material (referred to as GH4169 alloy). In study³⁴ the burn-off length is greater than 10 mm and the overall analysis was based on the friction surface contact between 2D rigid-to-plastic deformable bodies, in contrast to the 3D plastic-to-plastic deformable bodies employed as the friction surface contact in the current paper. It is further observed that the input LFW process parameters—implemented in Yang

et al.'s study—differ from the process parameters used for configuring different setups (J1 to J10) in the current paper.

Fig. 17 shows the FE modelling results of the axial shortening of the bottom workpiece of this paper compared to the practically measured axial shortening by Geng et al. ⁴⁴, based on the LFW setup J6. Both axial shortening results show a reasonable agreement. The original axial length of each workpiece is 33 mm. During LFW, this axial shortening length changes when the interface material thermo-plastically softens under the application of high compressive force. Thus, as shown in Fig. 17, the welding process from 1.0 s to 5.0 s shows progressive increment in the shortening length.

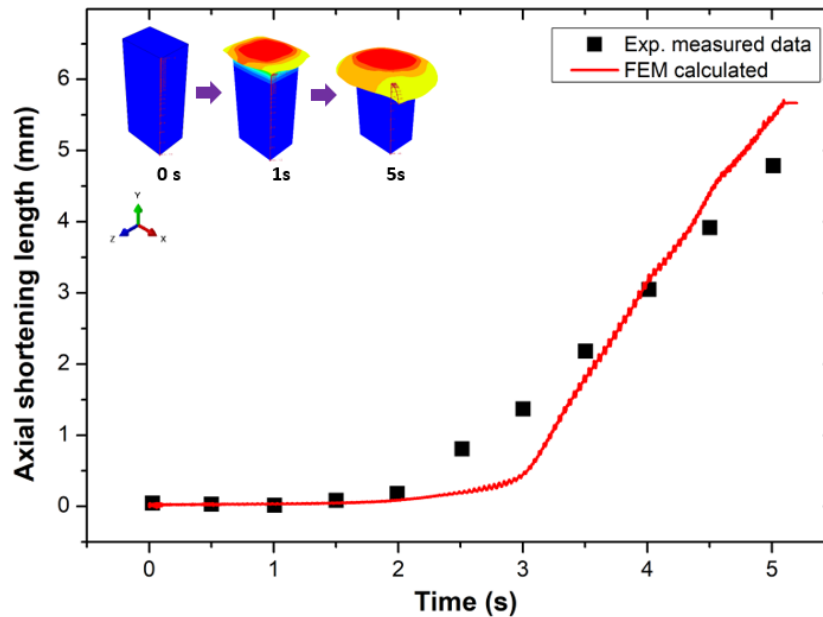


Figure 17. Comparative axial shortening of the FE model against experimentally measured data for a total welding time of 5 s for setup J6 ⁴⁴

Previous research ^{26, 27, 32, 33, 86} have reported on the benefit of sufficient shortening length for achieving defect-free weld joints; it corresponds to adequate extrusion of flash material as well as the elimination of oxides at the friction interface. Scholars investigating the computational modelling of the LFW of nickel-base superalloy ^{18, 33, 36, 50, 53, 87} have affirmed that by applying high forging force during LFW process, a self-cleaning effect is effected and high integrity weld joints are manufactured. A total shortening length of 5.95

mm was calculated for the setup J6 of the current study. With the same LFW process parameters for experimental iterations ($p_f = 400 \text{ MPa}$, $A_0 = 2.9 \text{ mm}$ and $f_0 = 25 \text{ Hz}$), Geng et al.³² recommended that axial shortening must be greater than 4.8 mm (critical shortening length) for a sound weld joint manufactured free of oxides at the interface. The FE modelling results shown in Figs. 16 and 17 provide clear evidence of the suitability of the present 3D fully coupled thermomechanical model for predicting shortening length during LFW.

3.6.3 Relationship between Mises stress, microhardness, and averaged gamma grain size

To adjudge that sound IN-718 alloy weld joints with optimal mechanical properties were developed, selected macroscale modelling results—such as temperature and stress—were correlated to the microstructure and mechanical properties of the weld joint that were characterised by Geng et al.^{32, 33} based on using the LFW setup J6. IN-718 is a solid-solution strengthened superalloy. Thus, the strengthening influences of refined grains and precipitate particles can significantly influence the microhardness of IN-718 superalloy^{19, 32, 33, 86}. The major strengthening phase has been reported to be a metastable gamma double-prime (γ'') phase, which usually precipitates at 550 — 900 °C^{32, 33, 85}. It can transform to the deleterious stable delta (δ) phase that deteriorates mechanical properties.

Fig. 18 shows the qualitative comparison between the FE modelling result of temperature profile of the weld of this paper and Geng et al.'s³² experimental results of the microhardness (HV) and averaged-size of γ grains (μm) of the weld in the weldline friction interface zone (FIZ) and thermomechanically-affected zone (TMAZ). These results are based on setup J6 that utilises friction pressure (p_f), oscillation amplitude (A_0) and oscillation frequency (f_0) of 400 MPa, 2.9 mm and 25 Hz, respectively. In Fig. 18, the horizontal axis represents the distance between the position of interest and the friction interface along the centre line of the weld for up to 3.5 mm. The continuous red curve presents this paper's finite element modelling results of the temperature profile of the weld as a function of the distance to the friction interface. The black curve and scattered triangular symbols represent the profile of the grain size, and the green curve and scattered circular symbols represent the profile of the hardness of the weld according to Geng et al.'s experimental results³².

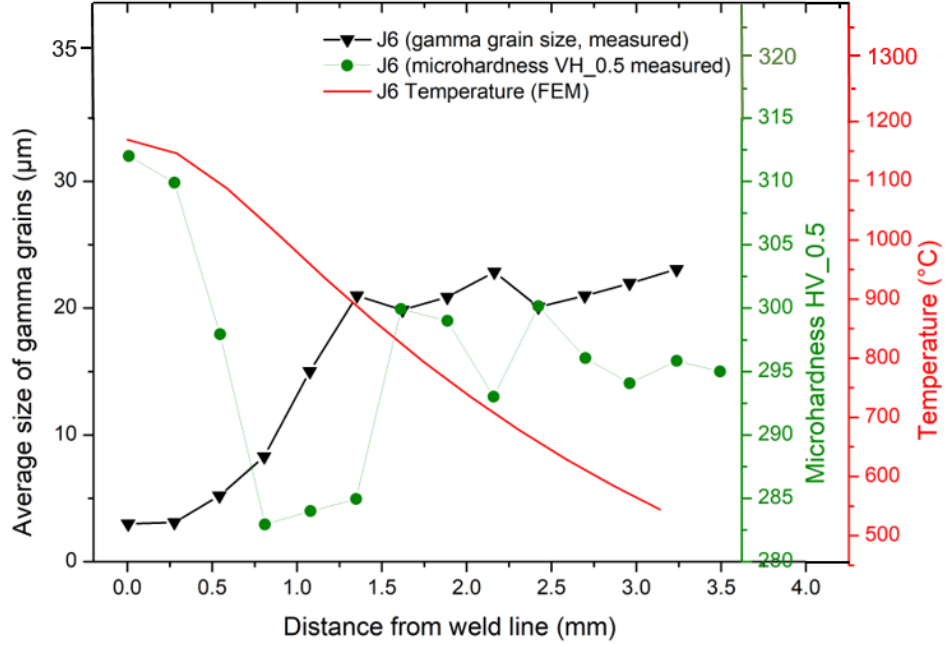


Figure 18. The profile of material microhardness and the averaged size of gamma grains experimentally measured by Geng et al. ³² and the FE modelling result of the temperature profile of the weld of this paper based on setup J6.

The maximum temperature is observed at the interface as 1165.4 °C and decreases to 550 °C at a distance of 3.2 mm from the weld line. Similarly, the maximum value of microhardness (312 HV) is observed at the interface, which decreases to a minimum value of 283 HV at approximately 1.0 mm from the weld line. From a distance of 1.5 mm to 1.6 mm, the microhardness increases from 285 HV to 303 HV, which is a region outside of the weld interface zone. In contrast, the average size of gamma grains increased from 3 µm at the interface to 22 µm at a distance of 1.4 mm from the weld line. The measured microhardness in the friction interface zone (FIZ) is evidently influenced by the weld temperature, which governs the combined influences of grain refinement and evolution of the strengthening phase. Geng et al. ³² and Masoumi et al. ²⁸ affirmed that the change in microstructure hardness within the FIZ and TMAZ can be attributed to the effect of fine-grain strengthening than the effect of dissolution of strengthening phase. Both fine grain-strengthening and dissolution strengthening are influenced by weld temperature. The

gamma (γ) grain size in the FIZ is continuously changing because of dynamic recrystallization (DRX).

Fig. 19 shows a maximum temperature value, maximum microhardness, and minimum Mises stress value at the weld interface. The microhardness of contacting surfaces rapidly decreases from the weld line to a distance of 1.0 mm from the interface without significant consequence to the LFW process up to 1.0 s of welding time. At 3.0 mm from the weld line, where the base metal is located, the result for setup J6 indicates that temperature is less than 500 °C, which corresponds to values of microhardness and averaged gamma (γ) grain size within the base metal. The influence of temperature on the Mises stress has previously been discussed and only presented here to show the relationship with microhardness at the friction interface zone.

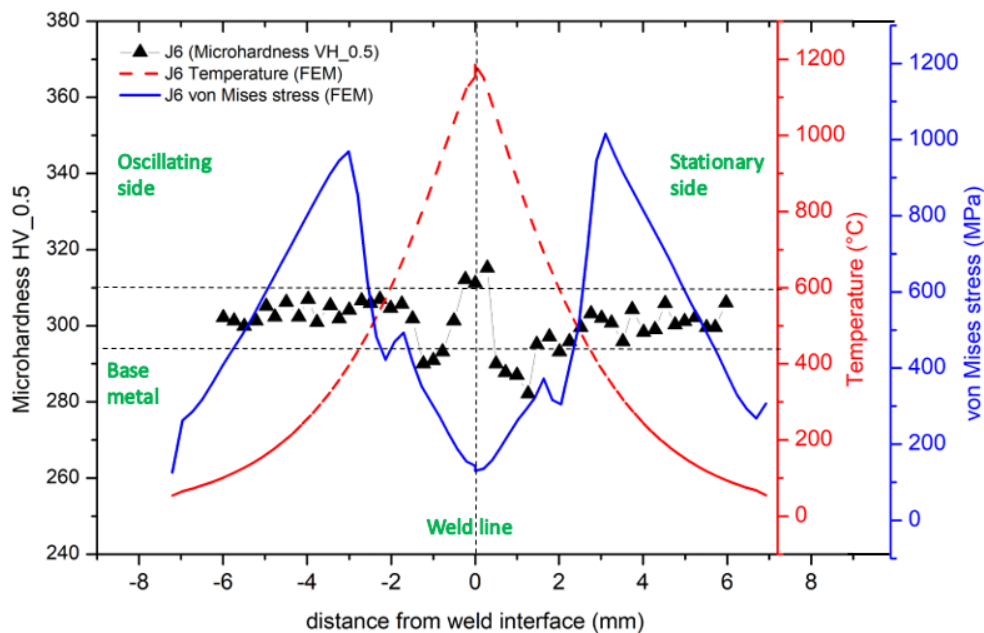


Figure 19. The evolution of microhardness (measured data)³² is compared to the evolution of temperature and von Mises stress across the friction interface for setup J6.

4. Summary and conclusions

In this paper, the influence of welding process parameters on the heat transfer and deformation of weld has been investigated by utilising a fully coupled three-dimensional thermomechanical modelling of the LFW process for two deformable plastic bodies of

IN718 alloy. The contributions of friction heat, plastic work, contact formulation, and constitutive material model have been taken into account to develop a highly accurate and predictive model. The following key conclusions can be drawn from this study:

- For the first time, a visible and systematic process window was determined for the LFW of two deformable bodies of Inconel 718 based on ten different setups (J1 to J10)
- In this process window, a broad range of optimal and sub-optimal input LFW process parameters were identified by comparing all weld interface thermal histories—from different simulated setups—against the liquidus temperature of IN718 superalloy
- Optimum specific power input was calculated within the range of values 3461.6 to 5769.4 kW. m⁻² for LFW input parameters within the range of values ($A_0 = 2.5$ to 3.5 mm, $f_0 = 25$ to 30 Hz and $p_f = 300$ to 500 MPa)
- The evolution of temperature on a specified location of the welded bottom workpiece was successfully validated against experimentally measured data
- Quantitative comparison of FEA displacement and deformation fields (flash geometry) showed high-level similarity to experimentally determined macrostructure LFW results
- Strong correlation and trends were shown between FE modelling results (Mises stress and temperature history) and experimentally measured data (microhardness and averaged grain size)

From the conclusions drawn, the developed computational model can potentially serve as a design and process optimisation tool to manufacture high-quality Inconel 718 alloy weld joints that exhibit appropriate material microstructure and optimal mechanical properties.

Data availability

The data used to support the findings of this study are available from the funding source on demand.

Declaration of conflicting interests

The authors declared no potential conflicts of interest with respect to the research, authorship, and/or publication of this article.

Acknowledgements

The authors gratefully acknowledge the enabling computational modelling platform provided by the Irish Centre for High-End Computing (ICHEC) Ireland.

Funding

The authors disclosed receipt of the following financial support for the research, authorship, and/or publication of this article: This publication has emanated from research supported in part by a research grant from Science Foundation Ireland (SFI) under [Grant Number 16/RC/3872] and is co-funded under the European Regional Development Fund. The authors gratefully acknowledge funding support by the National University of Ireland Galway doctoral scholarship.

ORCID iD

Saviour I. Okeke  <https://orcid.org/0000-0002-1664-4949>

References

1. Chamanfar A, Jahazi M and Cormier J. A Review on Inertia and Linear Friction Welding of Ni-Based Superalloys. *Metall Mater Trans A* 2015; 46a: 1639-1669.
2. McAndrew AR, Colegrove PA, Buhr C, et al. A literature review of Ti-6Al-4V linear friction welding. *Progress in Materials Science* 2018; 92: 225-257.
3. TWI. Linear Friction Welding Job Knowledge 146. <https://www.twi-global.com/technical-knowledge/job-knowledge/linear-friction-welding-146/> (2018, accessed 5 February 2018).
4. Vairis A. Investigation of frictional behaviour of various materials under sliding conditions. *Eur J Mech a-Solid* 1997; 16: 929-945.
5. Vairis A. FM. High frequency linear friction welding of a titanium alloy. *Wear* 1998; 217: 7-131.
6. Vairis A and Frost M. Modelling the linear friction welding of titanium blocks. *Mat Sci Eng a-Struct* 2000; 292: 8-17.
7. Ma T. J. TLF, Li W. Y., Zhang Y., Xiao Y., Vairis A. Linear friction welding of a solid-solution strengthened Ni-based superalloy: microstructure evolution and mechanical properties studies. *Journal of Manufacturing Processes* 2018; 34: 442–450.
8. Bhamji I, Preuss, M., Threadgill, P. L., and Addison, A. C. Solid state joining of metals by linear friction welding: a literature review. *Material Science and Technology* 2010; 27: 2-12.
9. Vishwakarma KR, Ojo, O. A., Wanjara, P., and Chaturvedi, M.C. Linear Friction Welding of Allvac® 718 Plus Superalloy. *7th International symposium on Superalloy 718 and Derivatives, TMS* 2010.
10. Vishwakarma K. R. O, O. A., Wanjara, P., Chaturvedi, M. C. Microstructural analysis of linear friction-welded 718 plus superalloy. *JOM* 2014; 66: 2525–2534.
11. Zhang LW, Pei, J. B., Zhang, Q.Z., Liu, C.D., Zhu, W.H., Qu, S. and Wang, J. H. . The Coupled FEM Analysis of the Transient Temperature Field during Inertia Friction Welding of GH4169 Alloy. *Acta Metallurgica Sinica (English Letters)* 2007; 20: 301-306.
12. Bhamji I, Addison, A. C., Threadgill, P. L., and Preuss, M. . Linear Friction Welding in Aerospace Engineering. (2012).
13. Li WY, Vairis A, Preuss M, et al. Linear and rotary friction welding review. *Int Mater Rev* 2016; 61: 71-100.
14. Ola OA, Ojo, O. A., Wanjara, P., Chaturvedi, M. C. Enhanced resistance to weld cracking by strain-induced rapid solidification during linear friction welding. *Philos Mag Lett* 2011; 91: 140-149.
15. Saboori A, Aversa A, Marchese G, et al. Application of Directed Energy Deposition-Based Additive Manufacturing in Repair. *Appl Sci-Basel* 2019; 9: 1-26.
16. Mateo-Garcia AM. BLISK Fabrication by Linear Friction Welding. *Advances in Gas Turbine Technology* 2011: 411-434.
17. Smith MM. *Characterization of linear friction welded in-service Inconel 718 superalloy* University of British Columbia, Canada, 2017.
18. Smith M, Bichler, L., Gholipour, J., Wanjara, P. Mechanical properties and microstructural evolution of in-service Inconel 718 superalloy repaired by linear friction welding. *International Journal of Advanced Manufacturing Technology* 2017; 90: 1931–1946.

19. Mary C, Jahazi, M. Multi-scale analysis of IN-718 microstructure evolution during linear friction welding. *Adv Eng Mater* 2008; 10: 573-578.
20. Grant B, Preuss M, Withers PJ, et al. Finite element process modelling of inertia friction welding advanced nickel-based superalloy. *Mat Sci Eng a-Struct* 2009; 513-14: 366-375.
21. Bhadeshia HKDH and DebRoy T. Critical assessment: friction stir welding of steels. *Science and Technology of Welding and Joining* 2009; 14: 193-196.
22. Huang Z. W. LHY, Baxter G., Bray S., Bowen P. Electron microscopy characterization of the weld line zones of an inertia friction welded superalloy. *J Mater Process Technol* 2011; 211: 1927-1936.
23. Guo Y. JT, Chiu Y. L., Li H. Y., Bray S., Bowen P. Microstructure and microhardness of Ti6246 linear friction weld. *Material Science and Engineering A* 2013; 562: 17-24.
24. Damodaram R. RSGS, Rao K. P. Microstructure and mechanical properties of friction welded alloy 718. *Material Science and Engineering A* 2013; 560: 781–786.
25. Yang J. *Microstructure-property development in linear friction welding of nickel-based superalloys*. The University of Birmingham, 2014.
26. Fratini L, Buffa G, Campanella D, et al. Investigations on the linear friction welding process through numerical simulations and experiments. *Mater Design* 2012; 40: 285-291.
27. Grujicic, M., Yavari R, Snipes JS, et al. Linear Friction Welding Process Model for Carpenter Custom 465 Precipitation-Hardened Martensitic Stainless Steel. *J Mater Eng Perform* 2014; 23: 2182-2198.
28. Masoumi F. SD, Jahazi M., Cormier J., Flipo B. C. D. . On the occurrence of liquation during linear friction welding of Ni-based superalloys. *Metallurgical and Materials Transactions A* 2017; 48: 2886–2899.
29. Masoumi F. TL, Shahriari D., Jahazi M., Cormier J., Devaus A., et al. High temperature creep properties of a linear friction welded newly developed wrought Ni-based superalloy. *Material Science and Engineering A* 2018; 710: 214–226.
30. Grujicic M, Yavari R, Snipes JS, et al. A linear friction welding process model for Carpenter Custom 465 precipitation-hardened martensitic stainless steel: A weld microstructure-evolution analysis. *Proceedings of the Institution of Mechanical Engineers, Part B: Journal of Engineering Manufacture* 2014; 229: 1997-2020.
31. Ma T. J. CX, Li W. Y., Yang X. W., Zhang Y., Yang S. Q. Microstructure and mechanical property of linear friction welded nickel-based superalloy joint. *Material and Design* 2016; 89: 85-93.
32. Geng P, Qin G, Li T, et al. Microstructural characterization and mechanical property of GH4169 superalloy joints obtained by linear friction welding. *Journal of Manufacturing Processes* 2019; 45: 100-114.
33. Masoumi F, Shahriari D, Monajati H, et al. Linear friction welding of AD730™ Ni-base superalloy: Process-microstructure-property interactions. *Mater Design* 2019; 183.
34. Yang XW, Li WY, Li JL, et al. Finite element modeling of the linear friction welding of GH4169 superalloy. *Mater Design* 2015; 87: 215-230.
35. Buhr, C., Ahmad, B., Colegrove, P. A., et al. Prediction of residual stress within linear friction welds using a computationally efficient modelling approach. *Mater Design* 2018; 139: 222-233.

36. L. Y. *Modelling of the Inertia Welding of Inconel 718*. The University of Birmingham 2010.
37. Li WY, Ma TJ and Li JL. Numerical simulation of linear friction welding of titanium alloy: Effects of processing parameters. *Mater Design* 2010; 31: 1497-1507.
38. Dechao, P. Z., Z, L. F. Numerical simulation of transient temperature and axial deformation during linear friction welding between TC11 and TC17 titanium alloys. *Computational Materials Science* 2014; 92: 325-333.
39. Zhao PK, Fu L and Zhong DC. Numerical simulation of transient temperature and axial deformation during linear friction welding between TC11 and TC17 titanium alloys. *Computational Materials Science* 2014; 92: 325-333.
40. Vairis, A., C, N. The development of a continuum framework for friction welding processes with the aid of micro-mechanical parameterisations. *International Journal of Modelling, Identification and Control* 2007; 2: 347-355.
41. Song X. *Modelling Residual Stresses and Deformation in Metal at Different Scales*. University of Oxford, Oxford, England, 2010.
42. Bühr, C. CPA, McAndrew A. R. A computationally efficient thermal modelling approach of the linear friction welding process. *J Mater Process Technol* 2018; 252: 849–858.
43. McAndrew A. R. C, P. A., Addison, A. C., Flipo, B. C. D., Russell, M. J. Energy and force analysis of Ti-6Al-4V linear friction welds for computational modeling input and validation data. *Metallurgical and Materials Transactions A* 2014; 45: 6118-6128.
44. Geng, P. H., Qin, G. L., Chen, L., et al. Simulation of plastic flow driven by periodically alternating pressure and related deformation mechanism in linear friction welding. *Mater Design* 2019; 178.
45. Wang X, Li W, Ma T, et al. Effect of welding parameters on the microstructure and mechanical properties of linear friction welded Ti-6.5Al-3.5Mo-1.5Zr-0.3Si joints. *Journal of Manufacturing Processes* 2019; 46: 100-108.
46. Maalekian, M. KE, Brantner H. P., Cerjak H. Comparative analysis of heat generation in friction welding of steel bars. *Acta Materialia* 2008; 56: 2843–2855.
47. Sekhar N. C. RRC. Power beam welding of thick section nickel base superalloys. 2002; 7: 77-87.
48. Li WY, Wang FF, Shi SX, et al. Numerical Simulation of Linear Friction Welding Based on ABAQUS Environment: Challenges and Perspectives. *J Mater Eng Perform* 2014; 23: 384-390.
49. Grujicic, M. A, A. Pandurangan, B., Yen, C. F., and Cheeseman, B.A. . Process Modeling of Ti-6Al-4V Linear Friction Welding (LFW). *Journal of Materials Engineering Performance* 2012; 21: 2011-2023.
50. Qin GL, Geng PH, Zhou J, et al. Modeling of thermo-mechanical coupling in linear friction welding of Ni-based superalloy. *Mater Design* 2019; 172: 1-18.
51. McAndrew A. R. C, P. A., Flipo, B. C. D., and Bühr, C 3D modelling of Ti-6Al-4V linear friction welds. *Science and Technology of Welding and Joining* 2017; 22: 496-504.
52. Geng PH, Qin GL, Zhou J, et al. Finite element models of friction behaviour in linear friction welding of a Ni-based superalloy. *International Journal of Mechanical Sciences* 2019; 152: 420-431.

53. Geng P, Qin G and Zhou J. A computational modeling of fully friction contact-interaction in linear friction welding of Ni-based superalloys. *Mater Design* 2020; 185.
54. P. Geng GQ, T. Li, J. Zhou, Z. Zou. Hot deformation behavior and constitutive model of GH4169 superalloy for linear friction welding process. *Journal of Manufacturing Processes* 2018; 32: 469-481.
55. Bertrand S, Shahriari, D., Jahazi, M., Champiaud, H. Linear friction welding process simulation of Ti-6Al-4V alloy. *Procedia Manufacturing* 2018; 15: 1382-1390.
56. Moal A, Massoni, E. Finite element simulation of the inertia welding of two similar parts. *Engineering Computations* 1995; 12: 497-512.
57. Jacquin D, de Meester B, Simar A, et al. A simple Eulerian thermomechanical modeling of friction stir welding. *Journal of Materials Processing Technology* 2011; 211: 57-65.
58. Al-Badour F, Merah N, Shuaib A, et al. Coupled Eulerian Lagrangian finite element modeling of friction stir welding processes. *Journal of Materials Processing Technology* 2013; 213: 1433-1439.
59. Tongne A, Robe H, Desrayaud C, et al. Two Dimensional Coupled Eulerian Lagrangian (CEL) Model for Banded Structure Prediction In Friction Stir Welding With Trigonal Tool. *Aip Conf Proc* 2016; 1769.
60. Ansari MA, Samanta A, Behnagh RA, et al. An efficient coupled Eulerian-Lagrangian finite element model for friction stir processing. *The International Journal of Advanced Manufacturing Technology* 2018; 101: 1495-1508.
61. Dassault-Systèmes. Abaqus 6.14 Analysis User's Guide. Volumes I – V. 2014.
62. McAndrew A. R. C, P. A., Flipo, B. C. D., and Bühr, C. . 3D modelling of Ti-6Al-4V linear friction welds, *Science and Technology of Welding and Joining*. 2017; 22: 496-504.
63. McAndrew AR, Colegrove PA, Addison AC, et al. Modelling of the workpiece geometry effects on Ti-6Al-4V linear friction welds. *Mater Design* 2015; 87: 1087-1099.
64. Schröder F, Ward, R. M., Walpole, A. R., Attallah, M. M., Gebelin, J. C., Reed, R. C. Linear friction welding of Ti6Al4V: experiments and modelling. *Acta Metall* 2015; 3: 372-384.
65. Turner R, Gebelin JC, Ward RM, et al. Linear friction welding of Ti-6Al-4V: Modelling and validation. *Acta Materialia* 2011; 59: 3792-3803.
66. Yang X, Li W, Fu Y, et al. Finite element modelling for temperature, stresses and strains calculation in linear friction welding of TB9 titanium alloy. *J Mater Res Technol* 2019; 8: 4797-4818.
67. Buffa G, Cammalleri M, Campanella D, et al. Shear coefficient determination in linear friction welding of aluminum alloys. *Mater Design* 2015; 82: 238-246.
68. Li W. Y. W, F. F. Modeling of continuous drive friction welding of mild steel. *Material Science and Engineering A* 2015; 528: 5921-5926.
69. Li WY, Shi SX, Wang FF, et al. Heat reflux in flash and its effect on joint temperature history during linear friction welding of steel. *Int J Therm Sci* 2013; 67: 192-199.
70. Salloomi, K. N. Fully coupled thermomechanical simulation of friction stir welding of aluminum 6061-T6 alloy T-joint. *Journal of Manufacturing Processes* 2019; 45: 746-754.

71. Bu W., Liu, J. The coupled thermal-mechanical modeling of the inertia friction welding process for Inconel 718. *Materials Science Forum* 2012; 704-705: 710-716.
72. Du, S.G. DLY, Cheng S. G. Friction mechanism and friction coefficient in the initial phase of friction welding. *Mech Sci Technol* 1997; 4: 703–707.
73. Zhou N, Shen, C., Mills, M. J., Li J, Wang, Y. Z. Modeling dislocation–diffusion coupled dislocation shearing of γ' precipitates in Ni-base superalloy. *Acta Materialia* 2011; 59: 3484-3497.
74. Sims, C. T., Stoloff, N. S., Hagel, W.C. *Superalloys II*. New York: John Wiley & Sons, 1987.
75. Reed, R. C. *The Superalloys: Fundamentals and Applications*. Cambridge, England: Cambridge University Press, 2006.
76. Wang FF, Li WY, Li JL, et al. Process parameter analysis of inertia friction welding nickel-based superalloy. *International Journal of Advanced Manufacturing Technology* 2014; 71: 1909-1918.
77. Yang, X., Li, W., Ma, J., Hu, S., He, Y., Li, L., Xiao, B. Thermo-physical simulation of the compression testing for constitutive modeling of GH4169 superalloy during linear friction welding. *J Alloys Compd* 2015; 656: 395-407.
78. Baffari D, Buffa, G., Campanella, D., Fratini, L., Micari, F. Single block 3D numerical model for linear friction welding of titanium alloy. *Science and Technology of Welding and Joining* 2018: 1-6.
79. Ji SD, Wang Y, Liu JG, et al. Effects of welding parameters on material flow behavior during linear friction welding of Ti6Al4V titanium alloy by numerical investigation. *International Journal of Advanced Manufacturing Technology* 2016; 82: 927-938.
80. Yang XW, Li WY, Li J, et al. FEM analysis of temperature distribution and experimental study of microstructure evolution in friction interface of GH4169 superalloy. *Mater Design* 2015; 84: 133-143.
81. Li WY, Wang FF, Shi SX, et al. 3D Finite Element Analysis of the Effect of Process Parameters on Linear Friction Welding of Mild Steel. *J Mater Eng Perform* 2014; 23: 4010-4018.
82. Dassault-Systèmes. Abaqus 6.14 Example Problems Guide Volume 1. *Static and Dynamic Analyses*. Providence, RI, USA: Dassault Systèmes Simulia Corp., 2014.
83. H. Schmidt JH. A local model for the thermomechanical conditions in friction stir welding. *Modelling and Simulation in Materials Science and Engineering* 2005; 13: 77-93.
84. Buffa G, Fratini, L. Strategies for numerical simulation of linear friction welding of metals: a review. *Prod Eng-Res Dev* 2017; 11: 221-235.
85. Anderson MJ, Panwisawas C, Sovani Y, et al. Mean-field modelling of the intermetallic precipitate phases during heat treatment and additive manufacture of Inconel 718. *Acta Materialia* 2018; 156: 432-445.
86. Chamanfar A, Sarrat L, Jahazi M, et al. Microstructural characteristics of forged and heat-treated Inconel-718 disks. *Mater Design* 2013; 52: 791-800.
87. Chamanfar A, Jahazi M, Gholipour J, et al. Mechanical Property and Microstructure of Linear Friction Welded WASPALOY. *Metall Mater Trans A* 2011; 42a: 729-744.